



This is the accepted manuscript made available via CHORUS. The article has been published as:

Modeling boundary-layer transition in direct and large-eddy simulations using parabolized stability equations

A. Lozano-Durán, M. J. P. Hack, and P. Moin

Phys. Rev. Fluids **3**, 023901 — Published 21 February 2018

DOI: [10.1103/PhysRevFluids.3.023901](https://doi.org/10.1103/PhysRevFluids.3.023901)

Modeling boundary-layer transition in direct and large-eddy simulations using parabolized stability equations

A. Lozano-Durán, M. J. P. Hack,^{*} and P. Moin

Center for Turbulence Research, Stanford University, CA 94305, USA

(Dated: January 19, 2018)

Abstract

We examine the potential of the nonlinear parabolized stability equations (PSE) to provide an accurate yet computationally efficient treatment of the growth of disturbances in H-type transition to turbulence. The PSE capture the nonlinear interactions that eventually induce breakdown to turbulence, and can as such identify the onset of transition without relying on empirical correlations. Since the local PSE solution at the onset of transition is a close approximation of the Navier-Stokes equations, it provides a natural inflow condition for direct numerical simulations (DNS) and large-eddy simulations (LES) by avoiding nonphysical transients. We show that a combined PSE/DNS approach, where the pre-transitional region is modeled by the PSE, can reproduce the skin-friction distribution and downstream turbulent statistics from a DNS of the full domain. When the PSE are used in conjunction with wall-resolved and wall-modeled LES, the computational cost in both the laminar and turbulent regions is reduced by several orders of magnitude compared to DNS.

^{*} Corresponding author; mjph@stanford.edu

I. INTRODUCTION

Modeling of laminar-turbulent transition remains one of the key challenges in the numerical simulation of boundary layers, especially at coarse grid resolutions. Transition to turbulence strongly affects many aspects of high practical significance such as the distribution of wall-shear stress or surface heat transfer. Consequently, the accurate identification of the onset of transition becomes of foremost importance for reliable estimates of drag and surface temperature. The issue is particularly relevant in wall-modeled large-eddy simulations (WMLES), which require 10 to 100 times more grid points in the thin laminar region than in the turbulent regime to properly capture the amplification of disturbances preceding the breakdown to turbulence [see NASA Vision 2030, 40]. Our study analyzes the ability of the nonlinear parabolized stability equations (PSE) to provide an accurate and computationally-efficient inflow boundary condition for direct and large-eddy simulations of flat-plate H-type transition in order to alleviate the grid-point requirements in the pre-transitional zone.

Boundary-layer transition to turbulence describes a complex process which can advance through several distinct pathways. In the presence of relatively low levels of external perturbations, as found for instance at atmospheric conditions, the transition process often begins with the amplification of exponential instabilities. In zero-pressure-gradient (ZPG) boundary layers, exponential growth can occur via the Tollmien-Schlichting (TS) wave, a viscous instability that becomes active past a critical Reynolds number. The TS wave is initially most unstable at zero spanwise wavenumber and is as such unable to initiate the three-dimensional state associated with breakdown to turbulence. In so-called K-type transition [24], three-dimensionality is provided by an oblique mode of the same frequency as the TS wave while in H-type transition the TS wave is supplemented by subharmonic oblique mode [16]. The modulation of the Blasius boundary layer by the amplifying TS wave causes the oblique modes to rapidly amplify so that the latter can be interpreted as secondary instabilities of the TS wave. Bypass transition, which can outpace transition by exponential instabilities in the presence of moderate to high levels of external perturbations [e.g. 13, 20], describes another route to turbulence which is however not the subject of the present study.

Direct numerical simulation (DNS) of the Navier-Stokes equations has been frequently used as a tool to investigate transitional flows. However, its computational cost is unaffordable in most practical settings. In order to explore more computationally efficient

approaches, Sayadi & Moin [36] conducted wall-resolved LES (WRLES) of H- and K-type transitional boundary layers. They found that constant-coefficient models for the subgrid-scale stress tensor could not predict transition and the flow remained laminar at all stream-wise locations. The reasons were traced back to the non-negligible turbulent viscosity in the laminar region, which dampens the amplification of instabilities. Dynamic sub-grid scale models sufficiently reduced the turbulent viscosity in the laminar flow and allowed the growth of disturbances [36]. When the grid was fine enough, WRLES reproduced the skin-friction overshoot observed in DNS. However, these calculations still require a relatively large number of grid points to capture the growth of instabilities, of the order of $Re^{1.85}$, which is not very far from the DNS scaling $Re^{2.64}$, where Re is characteristic Reynolds number of the problem [7].

Additionally, most of the grid points in the three directions used in WRLES are clustered close to the wall and more savings are achieved by adopting the so-called wall-modeled LES. In this case, the wall-stress is directly imposed at the wall instead of the classic no-slip boundary condition in order to relieve the grid requirements [7]. However, most wall models are derived assuming a fully-developed turbulent state which overestimates the momentum drain at the wall in the laminar zone and triggers premature transition. To address the issue, Bodart & Larsson [2] proposed a sensor based on the resolved turbulent-kinetic-energy to switch off the wall-model eddy viscosity and revert to the no-slip condition when the flow above the wall is detected as laminar. The results were satisfactory, although a threshold parameter had to be prescribed to discern between laminar and turbulent flow. In two related studies on a flat-plate boundary-layer transition, Park & Moin [32] and Park & Moin [31] devised a new wall-model able to account for non-equilibrium effects. However, the sensor from Bodart & Larsson [2] and wall-normal DNS-like resolution were still necessary in the laminar and pre-transitional regions in order to achieve an accurate prediction of the transition location.

The PSE were introduced by Herbert [17] and Bertolotti *et al.* [1] as an effective means for studying the evolution of small disturbances in spatially evolving flows. The approach captures nonparallel effects and has opened new avenues to the analysis of the spatial growth of disturbances in slowly varying shear flows such as boundary layers, jets, and far wakes. Both linear and nonlinear forms of the PSE exist, see e.g. Esfahanian *et al.* [10] for a survey of differences. The nonlinear PSE account for interactions between modes that

eventually induce breakdown to turbulence. Starting from an initial disturbance field within the boundary layer, the nonlinear PSE allows the identification of the onset of transition without relying on empirical correlations or prescribed thresholds in contrast to Reynolds-averaged Navier-Stokes (RANS) equations models [e.g., 33] or alternative approaches based on linear stability theory such as the e^N method [19, 41].

The present study continues the work by Hack & Moin [12] and aims to combine the advantages of the PSE and LES to enable the efficient simulation of transitional boundary layers. In the laminar regime, the streamwise evolution of the instability waves is captured using the nonlinear form of the PSE. Once the flow begins to transition, the local PSE solution is used as the inflow boundary condition in direct and large-eddy simulations. We show that in the classic H-type transition scenario, coupled calculations of ‘PSE with DNS’, ‘PSE with WRLES’, and ‘PSE with WMLES’ are able to predict the location of transition and reproduce the correct physical behavior in both the pre-transitional and turbulent regions. When compared to simulations where DNS or WRLES are used to compute the flow solution along the entire domain, the computational cost is reduced by several orders of magnitude.

The paper is organized as follows. The PSE are revisited in Section II. Section III describes the numerical experiments used in our study. The results are presented in Section IV, which is further divided in three subsections corresponding to the analysis of the pre-transitional zone, the prediction of friction coefficient, and the study of the turbulent region. Final conclusions are offered in Section V.

II. PARABOLIZED STABILITY EQUATIONS FOR MODELING THE PRE-TRANSITIONAL REGION

The PSE were introduced by Herbert [17] and Bertolotti *et al.* [1] as a computationally efficient alternative to DNS in the study of convectively unstable flows such as laminar boundary layers. The PSE can incorporate both nonparallel and nonlinear effects and thus capture the flow physics more faithfully than classical stability theory based on the assumption of parallel flow. Comparisons of the amplification of instabilities in boundary layers between the PSE and DNS have been carried out by Bertolotti *et al.* [1] and Joslin *et al.* [21] and showed excellent agreement.

In the following, the streamwise, wall-normal and spanwise directions are denoted by x ,

y , and z , respectively. The derivation of the PSE for incompressible flow starts by decomposing the state vector, $\bar{\mathbf{q}}$, into a base state $(U, V, W, P)^\top$ and a perturbation component $(u, v, w, p)^\top$ such as $\bar{\mathbf{q}}(x, y, z, t) = \mathbf{Q}(x, y) + \mathbf{q}(x, y, z, t)$, where u, v, w and their upper-case versions are the streamwise, wall-normal and spanwise velocities, respectively, and p is the pressure. Introduction of this decomposition into the Navier-Stokes equations and subtraction of mean-flow terms yields

$$\frac{\partial \mathbf{u}}{\partial t} + \mathbf{U} \cdot \nabla \mathbf{u} + \mathbf{u} \cdot \nabla \mathbf{U} + \frac{1}{\rho} \nabla p - \frac{1}{Re} \Delta \mathbf{u} = -\mathbf{u} \cdot \nabla \mathbf{u} \quad (1)$$

$$\nabla \cdot \mathbf{u} = 0, \quad (2)$$

where ρ is the fluid density. The perturbation field is assumed periodic in the spanwise direction and time and is expressed in terms of a Fourier expansion. The streamwise variation of the disturbance is split into a fast-changing oscillatory component that is governed by a complex wavenumber, $\alpha(x)$, and a slowly changing shape function, $\hat{\mathbf{q}}(x, y)$. The full ansatz for the disturbance field thus becomes

$$\mathbf{q}(x, y, z, t) = \sum_{n=-N}^N \sum_{m=-M}^M \hat{\mathbf{q}}_{n,m}(x, y) \exp \left(i \int_0^x \alpha_{n,m}(\xi) d\xi + i n \beta z - i m \omega t \right), \quad (3)$$

where β is the real spanwise wavenumber of the disturbance and ω is its real frequency. All lengths are normalized by the boundary layer thickness at the inflow location x_0 of the computational domain and velocities are normalized by the free-stream convective speed at that location. The spanwise and temporal Fourier expansions are truncated at a finite number of N and M modes, respectively. The ambiguity arising from the streamwise variation of both $\hat{\mathbf{q}}$ and α is resolved via the constraint

$$\int_{\Omega_y} \hat{\mathbf{q}}_{n,m}^H \frac{\partial \hat{\mathbf{q}}_{n,m}}{\partial x} dy = 0, \quad (4)$$

where superscript H denotes transpose conjugate. This ensures that $\hat{\mathbf{q}}_{n,m}(x, y)$ varies slowly with the streamwise coordinate. Other normalization conditions are possible, although they have been shown to produce similar results [8, 14, 21]. Introducing the ansatz Eq. (3) and retaining terms up to order $\mathcal{O}(Re^{-1})$, the parabolized stability equations take the form,

$$\mathbf{A} \hat{\mathbf{q}}_{n,m} + \mathbf{B} \frac{\partial \hat{\mathbf{q}}_{n,m}}{\partial y} + \mathbf{C} \frac{\partial^2 \hat{\mathbf{q}}_{n,m}}{\partial y^2} + \mathbf{D} \frac{\partial \hat{\mathbf{q}}_{n,m}}{\partial x} = \hat{\mathbf{F}}_{n,m}. \quad (5)$$

The definitions of the operators \mathbf{A} , \mathbf{B} , \mathbf{C} and \mathbf{D} for a steady, three-dimensional base state $(U, V, W, P)^\top$ are

$$\mathbf{A} = \begin{pmatrix} r + \frac{\partial U}{\partial x} & \frac{\partial U}{\partial y} & 0 & i\alpha \\ 0 & r + \frac{\partial V}{\partial y} & 0 & 0 \\ \frac{\partial W}{\partial x} & \frac{\partial W}{\partial y} & r & i\beta \\ i\alpha & 0 & i\beta & 0 \end{pmatrix}, \quad \mathbf{B} = \begin{pmatrix} V & 0 & 0 & 0 \\ 0 & V & 0 & 1 \\ 0 & 0 & V & 0 \\ 0 & 1 & 0 & 0 \end{pmatrix},$$

$$\mathbf{C} = \begin{pmatrix} -\frac{1}{Re} & 0 & 0 & 0 \\ 0 & -\frac{1}{Re} & 0 & 0 \\ 0 & 0 & -\frac{1}{Re} & 0 \\ 0 & 0 & 0 & 0 \end{pmatrix}, \quad \mathbf{D} = \begin{pmatrix} U & 0 & 0 & 1 \\ 0 & U & 0 & 0 \\ 0 & 0 & U & 0 \\ 1 & 0 & 0 & 0 \end{pmatrix},$$

with $r = -im\omega + i\alpha_{n,m}U + in\beta W + \frac{1}{Re}(\alpha_{n,m}^2 + n^2\beta^2)$. The forcing term $\hat{\mathbf{F}}_{n,m}$ accounts for the nonlinear terms on the right-hand side of Eq. (1) and is evaluated via a fast Fourier transform. In order to keep the computational effort at a minimum, the marching procedure at first only considers modes that are part of the initial condition. Additional modes are included if the magnitude of the respective nonlinear term, $\hat{\mathbf{F}}_{n,m}$, exceeds a threshold which is set to 10^{-7} in the present study.

Note that the above form Eq. (5) of the parabolized stability equations is not fully parabolic, which makes the system ill-posed for a spatial-marching approach. Detailed analyses by Haj-Hariri [14] and Li & Malik [26] showed that the streamwise pressure gradient is the main contributor to the residual ellipticity. Following Day *et al.* [8], we alleviate this issue by introducing a damping factor $0 \leq \epsilon \leq 1$ such that

$$\frac{\partial p}{\partial x} = \sum_{m=-M}^M \sum_{n=-N}^N \left(i\alpha_{n,m} \hat{p}_{n,m} + \epsilon \frac{\partial \hat{p}_{n,m}}{\partial x} \right) \exp[i(n\beta z - m\omega t)]. \quad (6)$$

The present choice of $\epsilon = 0$ removes the slow contribution to the total pressure gradient while the fast part associated with the harmonic oscillation and the exponential growth of the instability is retained.

Homogeneous Dirichlet boundary conditions are used for regular modes with $n \times m \neq 0$ both at the wall and in the free-stream,

$$u_{n,m}, v_{n,m}, w_{n,m} = 0 \quad \text{at} \quad y = 0 \quad \quad u_{n,m}, v_{n,m}, w_{n,m} = 0 \quad \text{at} \quad y \rightarrow \infty. \quad (7)$$

In the case of the mean-flow distortion ($n = 0, m = 0$) mass conservation requires a non-zero wall-normal velocity in the free-stream, so that

$$u_{0,0}, v_{0,0}, w_{0,0} = 0 \quad \text{at} \quad y = 0 \quad \quad u_{0,0}, \frac{\partial v_{0,0}}{\partial y}, w_{0,0} = 0 \quad \text{at} \quad y \rightarrow \infty. \quad (8)$$

Several factors contribute to the increased computational efficiency of the PSE approach when compared to direct numerical simulations. First, the Fourier series in t and z from Eq. (3) are severely truncated. Furthermore, the decomposition of the streamwise derivative into a slow- and fast-changing part allows a coarser streamwise resolution since the grid only needs to resolve the former. Finally, the parabolic nature of the discretized equations permits the efficient solution via a marching procedure in x . The marching terminates when the iterative update of the wavenumber or solution of the nonlinear system fails to converge. This is typically related to the rapid growth of nonlinear effects and the limited length of the Fourier series which produce an inaccurate representation of the flow past the onset of transition.

The particular approach adopted for the flat-plate geometry in this work takes advantage of the spanwise homogeneity of the flow to expand the velocity field in Fourier series. Nevertheless, the PSE can also accomodate more general configurations involving complex geometries. For example, Herbert *et al.* [18] and Stuckert *et al.* [42] have implemented the PSE method in general curvilinear coordinates, and applications to swept wings can be found in Chang *et al.* [5], Wang *et al.* [43] and Haynes & Reed [15] among others. Other extensions of the PSE applicable in the absence of spanwise homogeneity are the surface-marching PSE [4, 25], which assumes slow-spatial variations in the spanwise direction, and the plane-marching PSE [3, 9, 30], where the base flow is strongly dependent on the cross-sectional coordinates. These extensions of method will be required in future works in order to extend the current analysis to more general scenarios.

III. NUMERICAL EXPERIMENTS

We consider a zero-pressure-gradient flat-plate boundary layer from laminar to turbulent flow through H-type transition [17]. Unless otherwise stated, velocities are non-dimensionalized by the free-stream velocity, U_∞ . Wall units are denoted by superscript $+$ and defined in terms of u_τ , ν , and δ , where $u_\tau \equiv \sqrt{\nu \frac{\partial U}{\partial y}|_{y=0}}$ is the friction velocity, ν is the

kinematic viscosity of the flow, and δ is the boundary-layer thickness at 99% of U_∞ . We define δ_0 as δ at the inlet location. The Reynolds number based on the distance from the leading edge and the momentum thickness are denoted by Re_x and Re_θ , respectively.

In all cases, transition is triggered by imposing an inflow condition consisting of the Blasius solution plus disturbances obtained from the local Orr-Sommerfeld/Squire problem. In particular, we prescribe the disturbance in terms of a fundamental TS wave and a subharmonic oblique wave at $Re_x = 1.8 \times 10^5$. The fundamental non-dimensional frequency of the TS wave is $2F = \omega\nu/U_\infty^2 = 1.2395 \times 10^{-4}$, and the subharmonic frequency is set to F . Following Joslin *et al.* [21], the root-mean-squared amplitudes of the fundamental and subharmonic disturbances are 0.0048 and 0.145×10^{-4} , respectively, and the spanwise wavenumber of the latter is $\beta\delta_0 = 0.6888$. Regarding the remaining boundary conditions, the Blasius solution is used at the top of the computational domain and a convective boundary condition with convective velocity U_∞ is applied at the outlet [34]. The spanwise direction is periodic.

The length, height and width of the simulated box are $L_x = 305\delta_0$, $L_y = 30\delta_0$ and $L_z = 20\delta_0$. At the outlet, $\delta/\delta_0 \approx 6$, which is comparable to those used in earlier studies [37, 39]. All computations were run for 10 periods of the fundamental frequency (after transients) with 100 velocity fields stored per period and equally spaced in time.

We will investigate the potential of the PSE for modeling the pre-transitional region through six numerical experiments named as DNS-DNS, PSE-DNS, PSE-WRLES, CLES-CLES, WMLES-WMLES and PSE-WMLES. The first part of the name denotes the approach used to compute the pre-transitional zone (with the same inflow condition as described above). The second part is the method employed to calculate the transitional and turbulent regions. CLES is equal to WMLES but imposing the no-slip boundary condition at the wall, and C denotes ‘coarse’. The corresponding grid resolution and number of degrees of freedom of each case are summarized in Table I. Seven modes were used for solving the PSE in all of the cases. The domain decomposition for the six experiments is sketched in Figure 1. The matching location between PSE and DNS/WRLES is set at $Re_x = 4.0 \times 10^5$, while for PSE-WMLES it is located at $Re_x = 5.0 \times 10^5$. The choice of the two different locations will be discussed in detail later. For now, we can briefly mention that the PSE provide the flow from the inlet location up to $Re_x = 5.0 \times 10^5$. At this stage, the amplitudes of the disturbances computed with the PSE grow very rapidly which can be seen as an in-

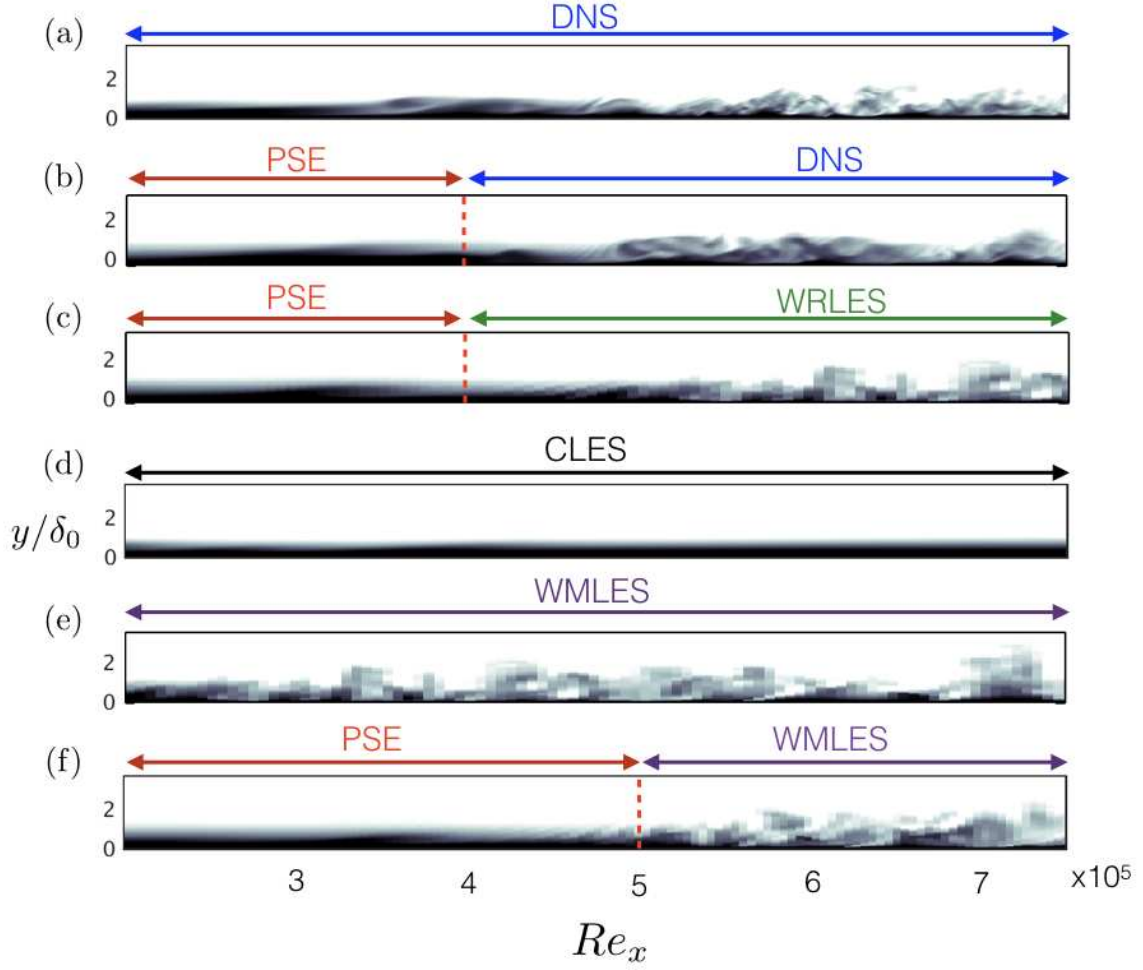


FIG. 1. Sketches of zero-pressure-gradient flat-plate transitional boundary layers for the six cases under consideration. Note that the flow from each panel is not plotted at comparable times. Colors represent streamwise velocity from zero (black) to free-stream velocity (white). The arrows and dashed red lines delimit the regions where different methodologies are used to compute the flow solution. (a) DNS-DNS case, (b) PSE-DNS case, (c) PSE-WRLES case, (d) CLES-CLES case, (e) WMLES-WMLES case, (f) PSE-WMLES case. The exact matching location between PSE and DNS/WRLES is at $Re_x = 4.0 \times 10^5$, and for PSE and WMLES at $Re_x = 5.0 \times 10^5$. The actual details of the simulations are summarized in Table I.

indicator of the onset of transition. For cases PSE-DNS and PSE-WRLES, we are interested in computing the flow before it departs from the laminar solution. For that purpose, we choose the PSE solution at $Re_x = 4.0 \times 10^5$ as inflow condition. On the other hand, the wall-normal mesh in the PSE-WMLES case is too coarse to capture the fine details during

Case	Pre-transition				Transition+turbulence				
	Δx^+	Δy_{min}^+	Δz^+	N_{points}	Δx^+	Δy_{min}^+	Δz^+	N_{points}	N_{total}
DNS-DNS	7.2	0.3	5.1	100M	7.2	0.3	5.1	150M	250M
PSE-DNS	44.0	0.2	-	0.2M	7.2	0.3	5.1	150M	150.2M
PSE-WRLES	44.0	0.2	-	0.2M	45.0	1.0	22.0	4M	4.2M
CLES-CLES	45.0	18.1	22.0	2.6M	45.0	18.1	22.0	4M	6.6M
WMLES-WMLES	45.0	18.1	22.0	2.6M	45.0	18.1	22.0	4M	6.6M
PSE-WMLES	44.0	0.2	-	0.2M	45.0	18.1	22.0	0.8M	1.0M

TABLE I. Parameters of the different numerical experiments. Δx and Δz are the streamwise and spanwise grid spacings, and Δy_{min} is the minimum (closest to the wall) wall-normal resolution. For the PSE, seven spanwise Fourier modes are used. N_{points} is the number of million grid points for each particular region and case, and N_{total} is the total number of points in the full domain.

the transitional breakdown, and we will use the PSE solution at the last streamwise available location, that is $Re_x = 5.0 \times 10^5$.

A reference DNS simulation of the full domain is performed with identical inflow conditions as those used for PSE calculations in order to make meaningful comparisons. PSE-DNS is used to assess the suitability of PSE for treating the pre-transitional region. In the case PSE-WRLES, we combine PSE for the pre-transitional region and WRLES for the transitional and turbulent zones. We will explore further computational savings by using wall models as commonly required in most engineering applications of external flows. Cases CLES-CLES and WMLES-WMLES are used to investigate the deficiencies of wall models in transitional scenarios, and case PSE-WMLES is the wall-modeled counterpart of PSE-WRLES with a coarser grid in the wall-normal direction.

DNS and LES solutions are computed by integrating the incompressible Navier-Stokes equations with staggered second-order central finite differences approximations as described in Orlandi [29]. Time advancement is achieved by a third-order Runge-Kutta scheme [45], combined with the fractional-step procedure [23]. All LES are carried out with the dynamic Smagorinsky subgrid-scale model as in Germano *et al.* [11] and Lilly [27]. WMLES is performed with the equilibrium wall model from Kawai & Larsson [22]. The code is parallelized using Message Passing Interface with a global transpose from y - z to x - y planes.

For the PSE, a second-order backward discretization is used to advance the solution in x . The wall-normal discretization uses a spectral approach based on Chebyshev polynomials. Given the streamwise parabolic nature of the discretized PSE, the coupling between PSE and DNS/WRLES/WMLES is effectively imposed as an inflow boundary condition in the latter.

As an example of the flow structures obtained in the simulations, Figure 2 shows the emergence of the characteristic staggered configuration of transitional hairpin vortices for cases DNS-DNS and PSE-DNS [see also 35].

IV. RESULTS

A. Pre-transitional region

In this section, we analyze in detail the differences and similarities between DNS and PSE solutions in the pre-transitional region of the flow. For this purpose, we compare the spanwise and temporal Fourier transforms of the streamwise velocity fluctuations. We focus first on the two most representative modes, the fundamental and subharmonic waves defined in Section III as those corresponding to the temporal and spanwise wavenumber pairs $(2, 0)$ and $(1, 1)$, respectively, where the first component of the vector is the temporal wavenumber in terms of F , and the second component a multiple of the spanwise wavenumber β .

The results are presented in Figure 3(a,b) as a function of the streamwise and wall-normal coordinates. A more detailed comparison is shown in Figure 3 at y/δ_0 for u_{rms} maximum. The agreement between DNS and PSE is reasonably good and the latter capture the downstream evolution of the TS wave in addition to the exponential growth of the subharmonic mode. Our results are thus consistent with those from Joslin *et al.* [21], who also reported a good match between DNS and PSE in a much more extensive investigation. Furthermore, the resulting transitional hairpin vortices for the PSE-DNS case are visually indistinguishable from those obtained for the DNS-DNS case as shown in Figure 2.

In order to further assess the importance of the particular flow structure provided by the PSE solution in the PSE-DNS case, a test case with a modified inflow condition is considered. The new inflow was computed by imposing a random perturbation velocity field to the Blasius solution with the additional constraints of 1) equal mean kinetic energy in

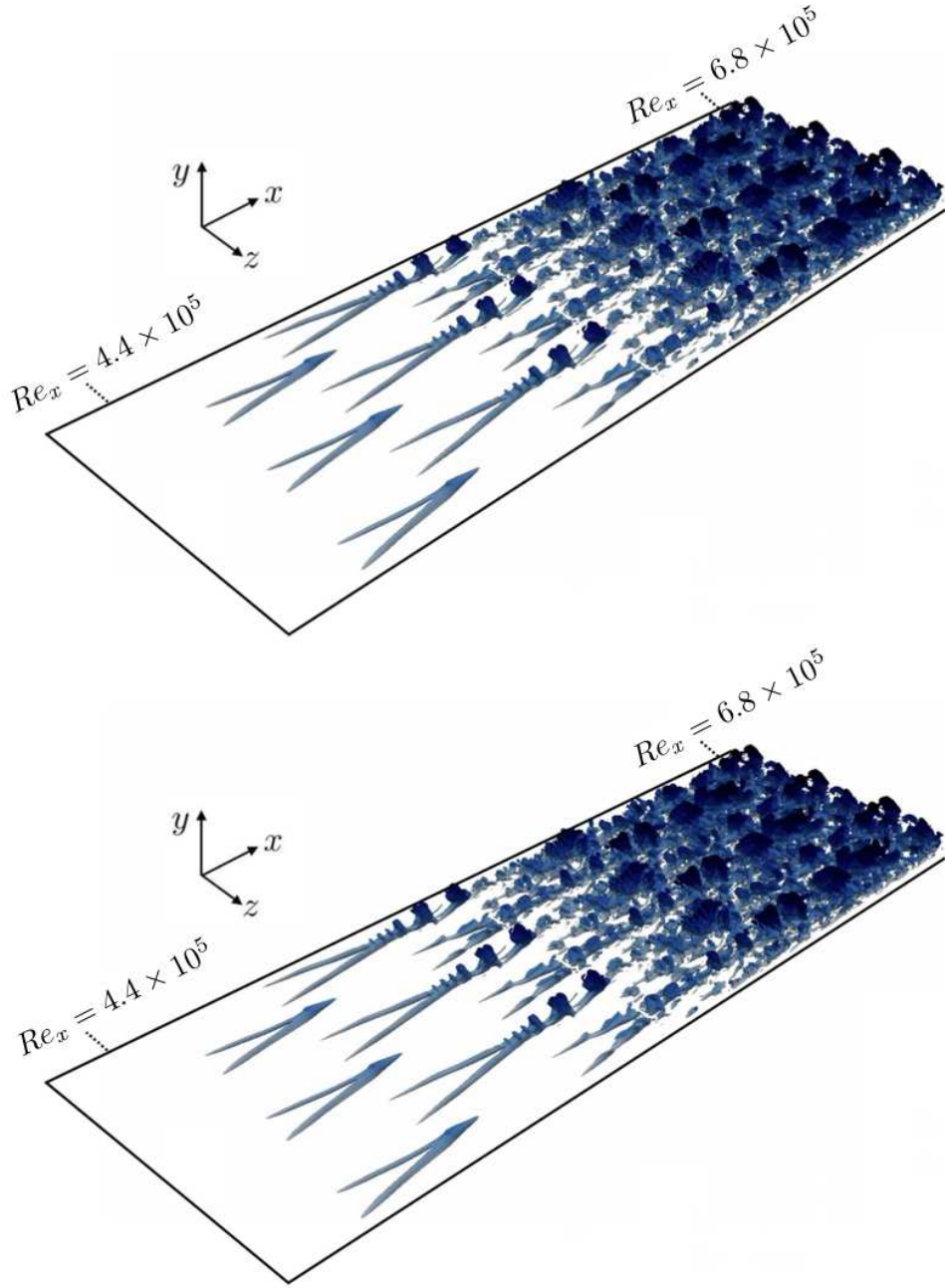


FIG. 2. Isocontours of positive instantaneous wall-normal velocity at a value of $3 \times 10^{-2} U_\infty$ at the same time. Top, DNS-DNS; bottom, PSE-DNS. Note that the spatial structure observed in (a) and (b) is almost identical even if (b) uses the PSE solution for the pre-transitional region up to $Re_x = 4 \times 10^5$.

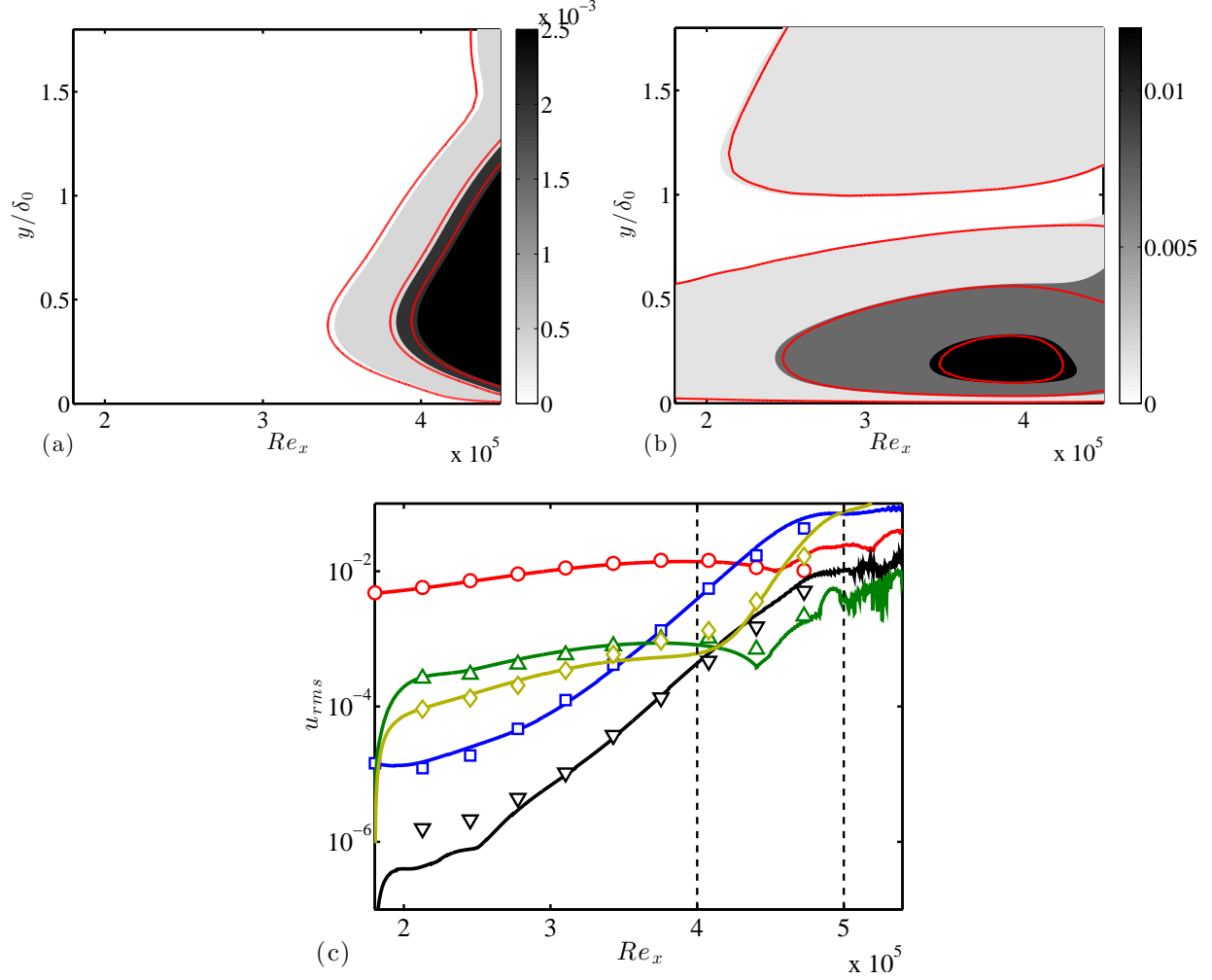


FIG. 3. Root-mean-square of the streamwise velocity Fourier modes as a function of Re_x and wall-normal distance. (a) Subharmonic mode (1,1) and (b) fundamental mode (2,0). Colors for the DNS-DNS case and solid red lines for PSE-DNS. Contours are 0.1, 0.5 and 0.9 of the maximum at $Re_x = 4.0 \times 10^5$. Panel (c) shows the root-mean-square of the streamwise velocity Fourier modes at y/δ_0 for maximum u_{rms} . Symbols are for PSE-DNS and modes (2,0), red circles; (1,1), blue squares; (0,0), yellow diamonds; (3,1), black upside-down triangles; (4,0), green triangles. Solid lines for DNS-DNS.

both wall-normal direction and time as the PSE solution, and 2) same number of spanwise and temporal modes as those of the original PSE inflow. Hence, the resulting solution has the same frequencies and energies as those computed from the PSE but lacks structural information. Isocontours of the instantaneous vertical velocity are shown in figure 4 at

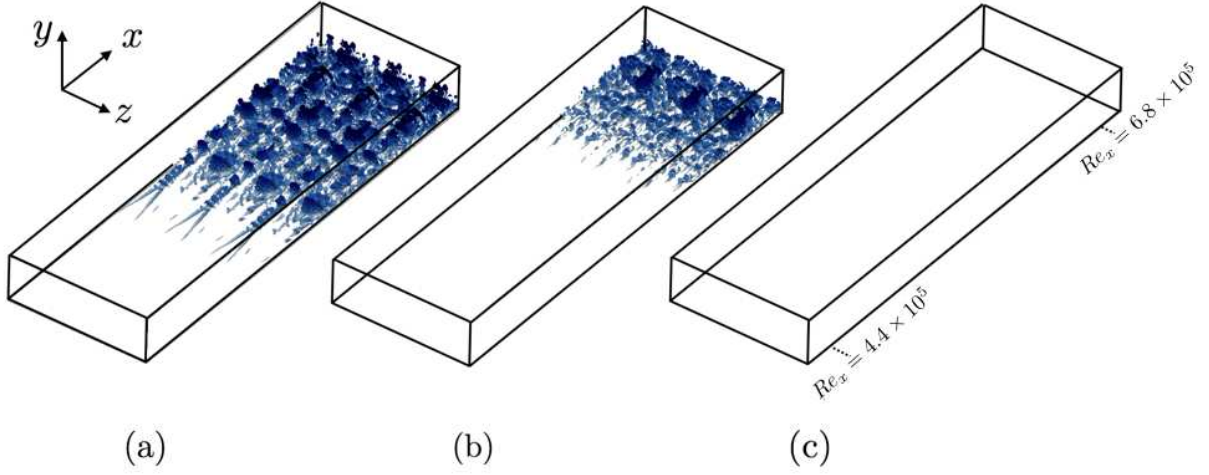


FIG. 4. Isocontours of positive instantaneous wall-normal velocity at a value of $3 \times 10^{-2} U_\infty$ for DNS-DNS with modified inflow condition at different times (a) $tU_\infty/\delta_0 = 0$, (b) $tU_\infty/\delta_0 = 86$ and (c) $tU_\infty/\delta_0 = 203$. The reference time is set to zero in figure (a), corresponding to the moment at which the inflow condition is switched from the PSE to randomized inflow (see text for details).

different instants after switching the inflow from PSE to the randomized version. The results show that the flow laminarizes completely after a few flow-throughs without transitioning again, at least along the limited streamwise length of our domain. This observation highlights the critical role of the PSE in accurately predicting the onset of transition by supplying a physically meaningful inflow velocity field.

B. Predicting the location of transition

In this section we will use the skin-friction coefficient C_f , defined as the non-dimensionalized mean wall-shear stress $2\tau_w/(\rho U_\infty^2)$, as a marker for detecting the transition to turbulence. The location of transition is commonly associated with the departure of the C_f from the laminar solution. We first discuss the prediction of transition for the DNS/WRLES cases,

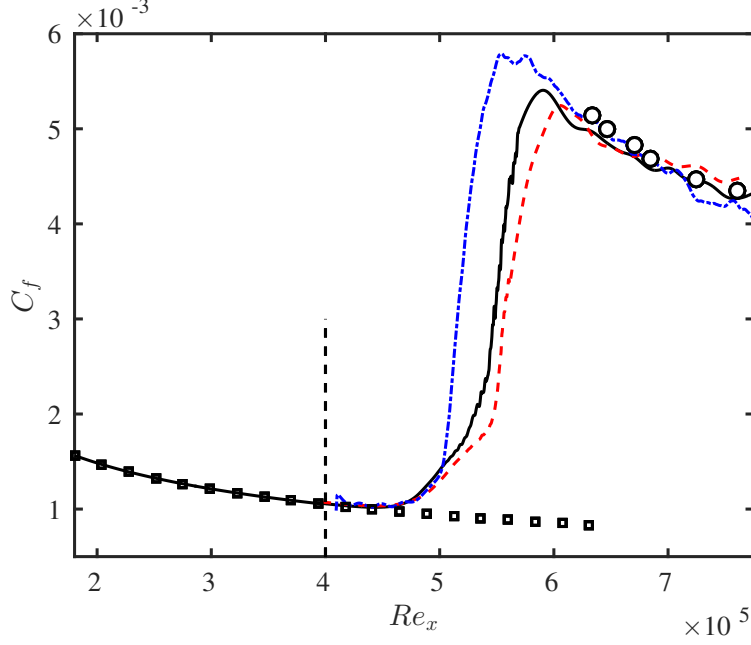


FIG. 5. Skin-friction coefficient as a function of the Reynolds number for cases involving DNS and WRLES. Solid black line, DNS-DNS; dashed red line, PSE-DNS; dash-dotted blue line, PSE-WRLES; black squares, Blasius correlation; circles, correlation from the DNS by Sayadi *et al.* [35]. The vertical dashed line is located at the coupling streamwise coordinate for PSE with DNS and WRLES.

and subsequently for those involving WMLES.

The streamwise distribution of C_f for the first three cases presented in Table I is reported in Figure 5. Since we are interested in solving the flow before the sudden increase of C_f , the matching location with the PSE solution is set at $Re_x = 4 \times 10^5$. In PSE-DNS, the onset of transition is accurately predicted compared to DNS-DNS despite the strong reduction in the number of degrees of freedom attained in the pre-transitional region (from 100M to 0.2M). The results demonstrate that the PSE faithfully account for the linear and nonlinear growth of disturbances that ultimately result in the breakdown of the laminar flow, in accordance with the accurate predictions of the different modes discussed in Section IV A. The transition location is still correctly captured in PSE-WRLES, which shows good agreement for the skin-friction coefficient in both the laminar and turbulent regions, even after reducing the total number of grid points by a factor of 60 (from 250M to 4.2M).

The above findings are in fundamental contrast to RANS-based approaches, which fail

to predict the correct location of the transition even with considerably higher number of grid points [33]. This is a consequence of the RANS averaging process, which eliminates the effects of linear disturbance growth and, therefore, commonly relies on empirical correlations to capture the onset of transition [28]. The same applies to other approaches such as the e^N method, which is not universal and need to be calibrated with experimental data [44]. For WRLES, it was shown by Sayadi & Moin [36] that constant-coefficient models also fail to differentiate between laminar and turbulent flows when WRLES is used in the entire domain, and the turbulent eddy-viscosity remains active throughout the whole domain inhibiting the growth of perturbations. Treatment of the pre-transitional region with the PSE avoids this issue. Another added advantage of adopting the PSE instead of WRLES for the laminar region is the reduction of the computational cost by at least an order of magnitude.

The most noteworthy deficiency of PSE-WRLES compared with DNS-DNS is the faster growth of the skin-friction coefficient in the transitional region, presumably due to the lack of resolution required to capture the full dynamic breakdown of the transitional hairpins. Figure 6 contains the instantaneous wall-normal velocity during transition for PSE-WRLES, and should be compared with its DNS-DNS counterpart in Figure 2. The WRLES resolution (see Table I) is fine enough to capture the transitional hairpins, although they are noticeably shorter in x . As the breakdown of the transitional hairpins was correctly represented in PSE-DNS, the issue is most likely related to the performance of the subgrid-scale model during transition rather than the inflow condition provided by the PSE solution.

Next, we discuss further computational savings by implementing a wall model. Results for C_f are shown in figure 7 for the three last cases from Table I. Figure 8 compares the instantaneous vertical velocity at a wall-parallel plane for DNS-DNS, CLES-CLES, WMLES-WMLES and PSE-WMLES. Cases WMLES-WMLES and CLES-CLES illustrate the main issues of WMLES and LES with coarse near-wall resolution. In both of them, the number of wall-normal grid points per boundary layer thickness in the turbulent region is chosen to be ~ 30 , which is sufficient for the accurate representation of the large-scale eddies in the outer region [6]. At the inlet, this corresponds to ~ 7 grid points. The near-wall region is under-resolved with a grid spacing $\Delta y^+ = 18.1$ at the wall. The equilibrium wall model is used in WMLES-WMLES, and CLES-CLES is computed using the same grid as WMLES-WMLES but imposing the no-slip boundary condition at the wall instead of the wall-stress from the wall model. Hence, CLES-CLES is a coarse LES near the wall and the flow never

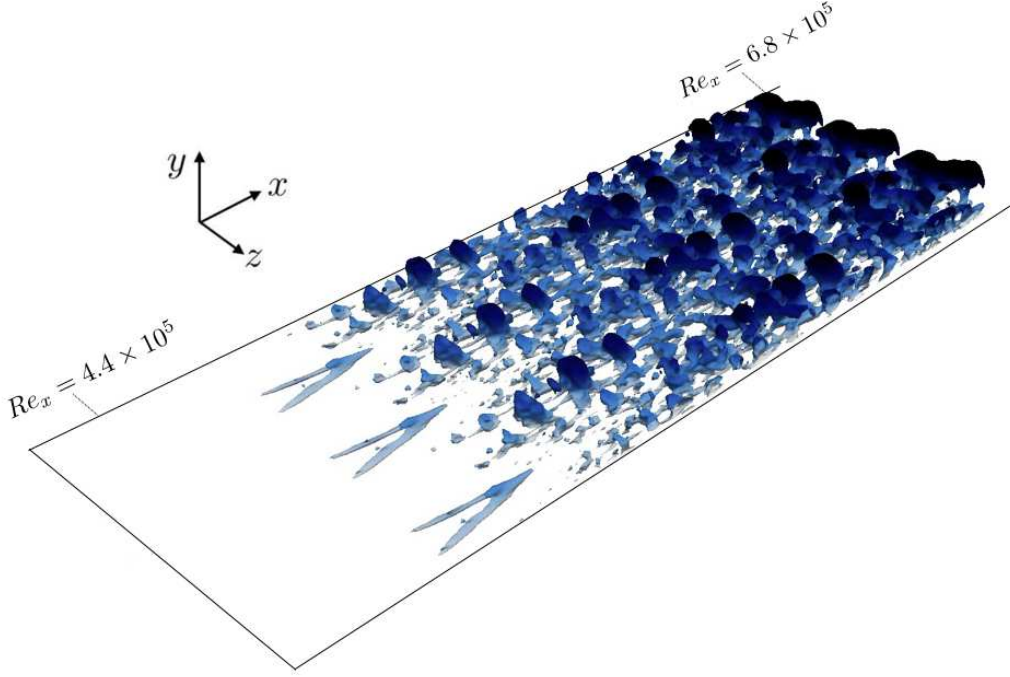


FIG. 6. Isocontours of positive instantaneous wall-normal velocity at a value of $3 \times 10^{-2}U_\infty$ for PSE-WRLES.

transitions from laminar to turbulent, presumably because the wall-normal resolution is insufficient to support the growth of the perturbations (figure 8b). In contrast, the presence of the wall model over the full extent of the domain in case WMLES-WMLES artificially triggers the breakdown to turbulence immediately after the inflow (figure 8c), as reported in previous studies [2]. The equilibrium wall-model, like most RANS-based approaches, uses a RANS eddy-viscosity in the near-wall layer consistent with an external turbulent flow. While this approximation has proven successful in many applications where the flow is fully turbulent, or even in non-equilibrium regimes, it drastically fails in laminar flows. In these cases, the overestimation of the momentum drain at the wall causes a premature transition. To address this deficiency, Bodart & Larsson [2] introduced a sensor based on the turbulent-kinetic-energy to switch off the RANS eddy-viscosity of the wall model and revert to the no-slip condition when the flow above the wall was identified as laminar. Case PSE-WMLES (figure 8d) alleviates the problem without the need of a sensor by explicitly treating most of the laminar region using the PSE, with the extra advantage of further reducing the cost by a factor of 6 compared to the WMLES-WMLES case. The outcome

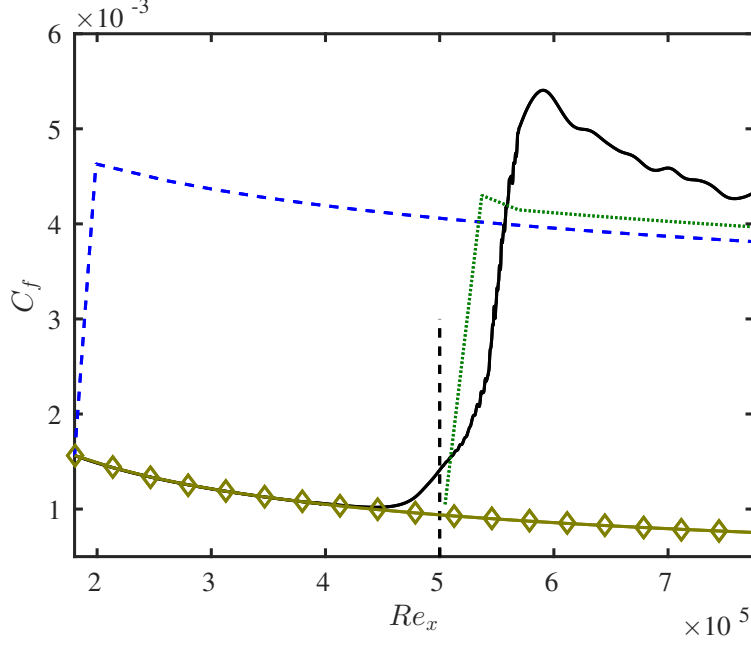


FIG. 7. Skin-friction coefficient as a function of the Reynolds number for cases involving DNS and WMLES. Solid black line, DNS-DNS; dashed blue, WMLES-WMLES; dotted green, PSE-WMLES; CLES-CLES, diamonds. The vertical dashed line is located at the coupling streamwise coordinate for PSE with WMLES.

represents a substantial improvement over CLES-CLES and WMLES-WMLES, where C_f was under- and over-predicted with an error larger than 200%.

Although unrelated to the PSE inflow condition, the characteristic C_f overshoot during transition is still under-predicted in PSE-WMLES. This is probably due to the inability of the equilibrium wall-model to capture the wall-footprint of the transitional hairpins after their breakdown. The issue is again related to the inconsistency between the fully-developed turbulent state assumed by the wall model and the actual structure of the transitional flow. The C_f overshoot was well predicted in Park & Moin [31, 32] and Bodart & Larsson [2]. However, these computations were carried out with wall-normal DNS-like resolution along the transitional region where the wall model was inactive.

Finally, we can discuss now the choice of the matching location with the PSE taking into account the results presented above. Due to the fast breakdown of the flow in the WMLES region, the streamwise location of the inflow for case PSE-WMLES is set just before the PSE solution diverges, that is $Re_x = 5 \times 10^5$, differently from the DNS and WMLES cases, where

the coupling is at $Re_x = 4 \times 10^5$. The reason is that in the last two cases, the PSE is in charge of providing the correct flow structure before the onset of transition, while in PSE-WMLES the role of the PSE is just to estimate the onset of transition. In this last case, the flow structure is diminished for two reasons, first, the mesh along the y coordinate is too coarse to capture the wall-normal details of the PSE solution and, second, the wall model forces the transition regardless of the particular flow structure imposed at the coupling point between the PSE and WMLES. This is different for the wall-resolved cases, which are highly sensitive to small changes in the inflow condition. For that reason, even minute deviations between the PSE and DNS solutions immediately before the breakdown to turbulence can shift the transition region. Preliminary calculations (not shown) pointed out that the streamwise matching location between PSE and DNS/WRLES needs to be approximately 40δ from the PSE breakdown region in order to obtain accurate predictions.

C. Turbulent region

In this last section we evaluate the performance of PSE-WRLES and PSE-WMLES in the turbulent region right after the transition. Some test cases not reported here suggest that after the breakdown of the transitional hairpin vortices, the role of the LES becomes more prominent on the first-order statistics of the flow in the turbulent region than the particular structure of the inflow solution computed from the PSE. This observation is further supported by previous works on flat-plate boundary-layer transition where different tripping methods converge to the same turbulent average solution once the memory of the upstream conditions has faded [38]. It follows that beyond the breakdown to turbulence, the influence of the PSE solution rapidly diminishes. Despite the secondary role of PSE in the turbulent region, the analysis is still relevant since both PSE and WRLES/WMLES must interact accordingly in the first stages after the transition in order to produce realistic turbulence.

Figure 9 compares the mean streamwise velocity profile and rms fluctuating velocities at $Re_\theta = 987$ ($Re_x \approx 7 \times 10^5$). Velocities and lengths are scaled in local wall units. Both the mean and rms velocities exhibit good agreement. Some differences appear in the mean velocity profile close to 10% in the wake region, although such an error can be argued to be acceptable given the aggressive reduction in the number of degrees of freedom, which is

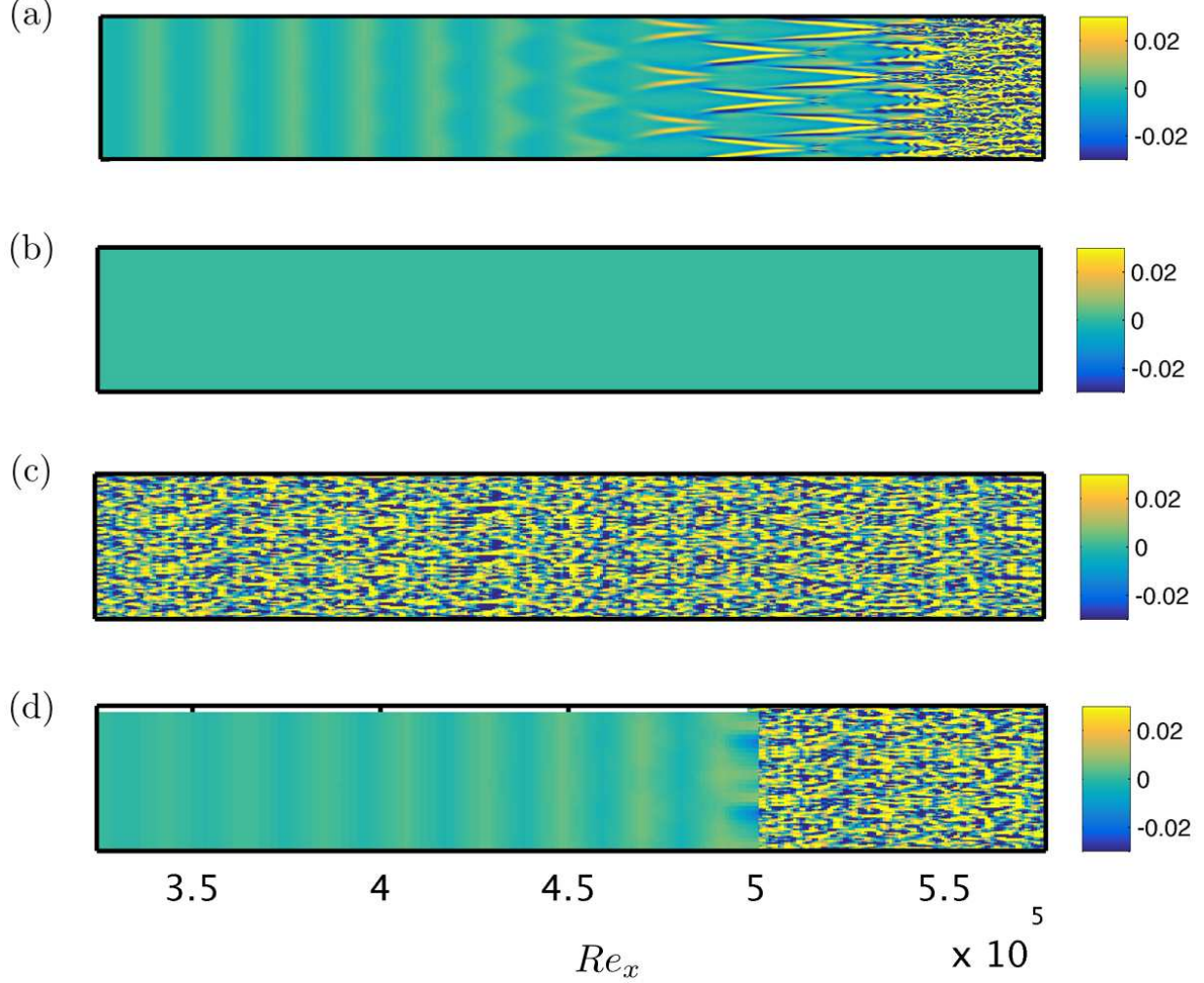


FIG. 8. Instantaneous vertical velocity at a wall-parallel plane at $y^+ \approx 30$ with wall-units computed from case DNS-DNS. (a), DNS-DNS; (b), CLES-CLES; (c), WMLES-WMLES; (d), PSE-WMLES. Velocities are normalized by U_∞ .

of the order of 60 times smaller in favor of the PSE-WRLES approach, and 250 times in PSE-WMLES.

Since U_∞ is imposed as the top boundary condition in both DNS and LES, the aforementioned velocity deficit in the PSE-WRLES wake is a direct consequence of the inaccurate viscous stress at the wall, used to non-dimensionalize the mean velocity in wall units. The solution is slightly improved by introducing the wall model in case PSE-WMLES. Overall, both PSE-WRLES and PSE-WMLES provide comparable predictions, although the computational cost is lower for PSE-WMLES. As discussed in Section IV B, the deficiencies in

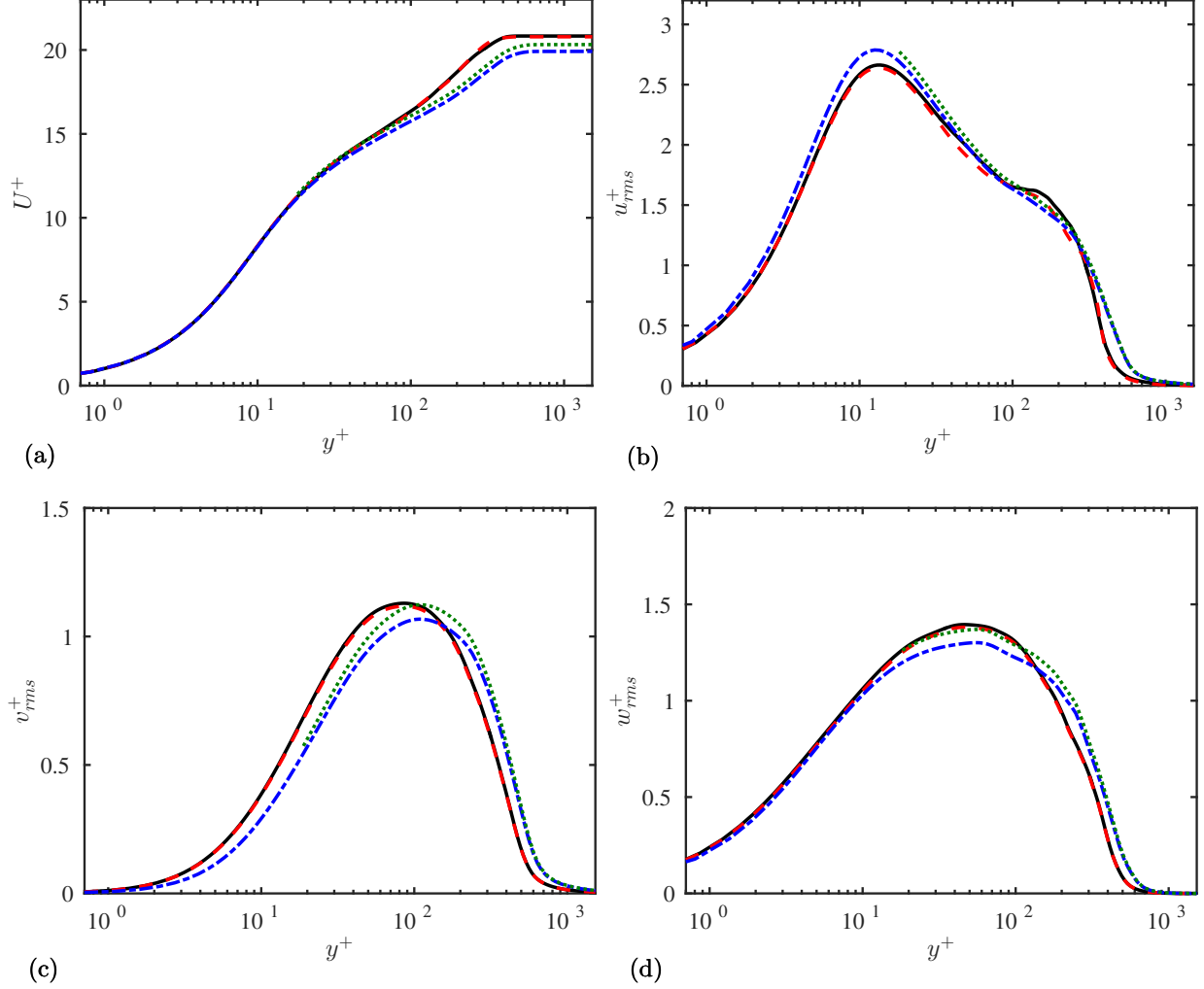


FIG. 9. (a) Mean streamwise velocity and (b) streamwise, (c), wall-normal and (d) spanwise root-mean-squared velocity fluctuations at $Re_\theta = 987$ ($Re_x \approx 7 \times 10^5$). Solid (black), DNS-DNS; dashed (red), PSE-DNS; dash-dotted (blue), PSE-WRLES; dotted (green), PSE-WMLES.

the turbulent region are unrelated to PSE, which has been shown to perform well in the PSE-DNS case, and future improvements in the turbulent region should focus on testing alternative wall models.

V. CONCLUSIONS

In the present study we have investigated the capabilities of the parabolized stability equations to provide accurate predictions in the zero-pressure-gradient boundary layer in the context of H-type transition.

A set of six computational experiments were performed to assess the suitability of the PSE to, first, model the disturbed laminar region and, second, act as an inflow condition in DNS, as well as in wall-resolved and wall-modeled LES just before the onset of transition. The results showed that the PSE-DNS combination is able to provide an accurate representation of the pre-transitional region, including the growth of the most significant modes and prediction of transition location, and correct one-point statistics in the turbulent region right after the flow breakdown. The importance of the particular solution provided by the PSE was established in a case where the PSE inflow condition was replaced by a randomized version with identical energy but different spatial flow configuration. Our results show that when the structure of the inflow is erroneous, transition is delayed and the flow laminarizes.

Further computational savings, of the order of 100 times compared with DNS, were achieved by combining the PSE with wall-resolved and wall-modeled LES for the transitional and turbulent zones while still reproducing the statistics with reasonable accuracy along the full boundary layer domain. For wall-resolved LES, the typical transitional hairpins are still present, although their breakdown is faster than in DNS. In the case of wall-modeled LES, the flow transitions prematurely when the wall model is active in the laminar region, and this issue is successfully addressed by modeling the laminar zone with the PSE. This approach avoids empirical correlations as well as the sensors often used to deactivate wall models before transition, with the additional advantage of further computational savings.

Acknowledgments

This investigation was funded by the Air Force Office of Scientific Research, NASA and Deutsche Forschungsgemeinschaft. The authors would like to acknowledge Drs. George Ilhwan Park and Aaron Towne for their fruitful comments.

-
- [1] BERTOLOTTI, F. P., HERBERT, T. & SPALART, P. R. Linear and nonlinear stability of the blasius boundary layer. *J. Fluid Mech.* **242**, 441 (1992).
 - [2] BODART, J. & LARSSON, J. Sensor-based computation of transitional flows using wall-modeled large eddy simulation. *Center for Turbulence Research Annual Research Briefs* 229 (2012).

- [3] BROADHURST, M. S. & SHERWIN, S. J. The parabolised stability equations for 3d-flows: Implementation and numerical stability. *Appl. Numer. Math.* **58** (7), 1017 (2008).
- [4] CHANG, C.-L. 2004 Lastrac.3d: Transition prediction in 3d boundary layer. *AIAA Paper* (2004).
- [5] CHANG, C.-L., MALIK, M. & VINH, H. Linear and nonlinear stability of compressible swept-wing boundary layers. *AIAA Pap.* (No 95-2278) (1995).
- [6] CHAPMAN, D. R. Computational aerodynamics development and outlook. *AIAA J.* **17**, 1293–1313 (1979).
- [7] CHOI, H. & MOIN, P. Grid-point requirements for large eddy simulation: Chapman’s estimates revisited. *Phys. Fluids.* **24** (1), 011702 (2012).
- [8] DAY, M. J., MANSOUR, N. N. & REYNOLDS, W. C. Nonlinear stability and structure of compressible reacting mixing layers. *J. Fluid Mech.* **446**, 375–408 (2001).
- [9] DE TULLIO, N., PAREDES, P., SANDHAM, N. D. & THEOFILIS, V. Laminar–turbulent transition induced by a discrete roughness element in a supersonic boundary layer. *J. Fluid Mech.* **735**, 613–646 (2013).
- [10] ESFAHANIAN, V., HEJRAFAR, K. & SABETGHADAM, F. Linear and nonlinear PSE for stability analysis of the Blasius boundary layer using compact scheme. *J. Fluids Eng.* **123**, 545 (2001).
- [11] GERMANO, M., PIOMELLI, U., MOIN, P. & CABOT, W. A dynamic subgrid-scale eddy viscosity model. *Phys. Fluids.* **3** (7), 1760 (1991).
- [12] HACK, M. J. P. & MOIN, P. Towards modeling boundary layer transition in large-eddy simulations. *Annual Research Briefs* pp. 137 (2015).
- [13] HACK, M. J. P. & ZAKI, T. A. Data-enabled prediction of streak breakdown in pressure-gradient boundary layers. *J. Fluid Mech.* **801**, 43 (2016).
- [14] HAJ-HARIRI, H. Characteristics analysis of the parabolized stability equations. *Stud. Appl. Math.* **92** (1), 41 (1994).
- [15] HAYNES, T. & REED, H. Computations in nonlinear saturation of stationary crossflow vortices in a swept-wing boundary layer. *AIAA Pap.* (No 96-0180) (1996).
- [16] HERBERT, T. 1988 Secondary instability of boundary layers. *Annu. Rev. Fluid Mech.* **20** (1), 487 (1988).
- [17] HERBERT, T. Boundary-layer transition - analysis and prediction revisited. *AIAA Pap.* **91**,

- 0737 (1991).
- [18] HERBERT, T., STUCKERT, G. & LIN, N. Method for transition prediction in high-speed boundary layers. *Wright Lab., Rep.* (WL-TR-93-3097) (1993).
 - [19] VAN INGEN, J. A suggested semi-empirical method for the calculation of the boundary layer transition region. *University of Technology, Department of Aerospace Engineering Report UTH-74* (1956).
 - [20] JACOBS, R. G. & DURBIN, P. A. Simulations of bypass transition. *J. Fluid Mech.* **428**, 185 (2001).
 - [21] JOSLIN, R. D., STREETT, C. L. & CHANG, C.-L. Spatial direct numerical simulation of boundary-layer transition mechanisms: Validation of PSE theory. *Theor. Comp. Fluid Dyn.* **4** (6), 271 (1993).
 - [22] KAWAI, S. & LARSSON, J. Wall-modeling in large eddy simulation: Length scales, grid resolution, and accuracy. *Phys. Fluids* **24** (1), 015105 (2012).
 - [23] KIM, J. & MOIN, P. Application of a fractional-step method to incompressible navier-stokes methods. *J. Comput. Phys* **59**, 308 (1985).
 - [24] KLEBANOFF, P. S., TIDSTROM, K. D. & SARGENT, L. M. The three-dimensional nature of boundary-layer instability. *J. Fluid Mech.* **12** (1), 1 (1962).
 - [25] LAKEBRINK, M. T., PAREDES, P. & BORG, M. P. Toward robust prediction of crossflow-wave instability in hypersonic boundary layers. *Comput. Fluids* **144** (Supplement C), 1 (2017).
 - [26] LI, F. & MALIK, M. R. On the nature of pse approximation. *Theoretical and Computational Fluid Dynamics* **8**, 253 (1996).
 - [27] LILLY, D. K. 1992 A proposed modification of the germano subgrid-scale closure method. *Phys. Fluids.* **4** (3), 633 (1992).
 - [28] MENTER, F. R., LANGTRY, R. & VÖLKER, S. 2006 Transition modelling for general purpose cfd codes. *Flow, Turbul. Combust.* **77** (1), 277 (2006).
 - [29] ORLANDI, P. *Fluid flow phenomena: A numerical toolkit, Fluid Mechanics and its Applications*, vol. 55, pp. 1 (2000).
 - [30] PAREDES, P., HANIFI, A., THEOFILIS, V. & HENNINGSON, D. S. The nonlinear pse-3d concept for transition prediction in flows with a single slowly-varying spatial direction. *Procedia IUTAM* **14** (Complete), 36 (2015).
 - [31] PARK, G. & MOIN, P. Numerical aspects and implementation of a two-layer zonal wall model

- for LES of compressible turbulent flows on unstructured meshes. *J. Comput. Phys.* **305**, 589 (2016).
- [32] PARK, G. I. & MOIN, P. An improved dynamic non-equilibrium wall-model for large eddy simulation. *Phys. Fluids* **26** (1), 015108 (2014).
- [33] PASQUALE, D., RONA, A. & S.J., G. A selective review of cfd transition models (2009).
- [34] PAULEY, L. L., MOIN, P. & REYNOLDS, W. C. The structure of two-dimensional separation. *J. Fluid Mech.* **220**, 397 (1990).
- [35] SAYADI, T., HAMMAN, C. W. & MOIN, P. Direct numerical simulation of complete H-type and K-type transitions with implications for the dynamics of turbulent boundary layers. *J. Fluid Mech.* **724**, 480 (2013).
- [36] SAYADI, T. & MOIN, P. Large eddy simulation of controlled transition to turbulence. *Phys. Fluids*. **24** (11), 114103 (2012).
- [37] SCHLATTER, P. & ÖRLÜ, R. Assessment of direct numerical simulation data of turbulent boundary layers. *J. Fluid Mech.* **659**, 116 (2010).
- [38] SCHLATTER, P. & ÖRLÜ, R. Turbulent boundary layers at moderate Reynolds numbers: inflow length and tripping effects. *J. Fluid Mech.* **710**, 5 (2012).
- [39] SILLERO, J., JIMÉNEZ, J. & MOSER, R. One-point statistics for turbulent wall-bounded flows at Reynolds numbers up to $\delta^+ \approx 2000$. *Phys. Fluids* **25** (10), 105102 (2013).
- [40] SLOTNICK, J., KHODADOUST, A., ALONSO, J., DARMOFAL, D., GROPP, W., LURIE, E. & MAVRIPLIS, D. *CFD Vision 2030 Study: A Path to Revolutionary Computational Aerosciences* (2014).
- [41] SMITH, A. & GAMBERONI, N. Transition, pressure gradients, and stability theory. *Douglas Aircraft Company* (Report No. ES-26388) (1956).
- [42] STUCKERT, G., HERBERT, T. & ESFAHANIAN, V. 1993 Stability and transition on swept wings. *AIAA Pap.* 93-0078 (1993).
- [43] WANG, M., HERBERT, T. & STUCKERT, G. PSE analysis of receptivity and stability in swept wing flows. *AIAA Pap.* No 94-0180 (1994).
- [44] WARREN, E. W. & HASSAN, H. A. Alternative to the e^n method for determining onset of transition. *AIAA J* **36**(1), 111 (1997).
- [45] WRAY, A. A. Minimal-storage time advancement schemes for spectral methods. *NASA-Ames Research Center, Moffett Field, CA* (private communication) (1986).